Journal of Nanobiotechnology

RESEARCH

Open Access

A metal-organic nanoframework for efficient colorectal cancer immunotherapy by the cGAS-STING pathway activation and immune checkpoint blockade

Xiaodian Zhang[1,2†], Hailong Tian[3†], Yang Chen[4†], Baichuan Liang[3], Edouard C. Nice[5], Canhua Huang[3], Na Xie[3*] and Shaojiang Zheng[1,2*]

Abstract

Immunotherapy has shown marked progress in promoting systemic anti-colorectal cancer (CRC) clinical effects. For further effectively sensitizing CRC to immunotherapy, we have engineered a pH-sensitive zeolitic imidazolate framework-8 (CS/NPs), capable of efficient cGAS-STING pathway activation and immune checkpoint blockade, by encapsulating the chemotherapeutic mitoxantrone (MTX) and immunomodulator thymus pentapeptide (TP5) and tailoring with tumor-targeting chondroitin sulfate (CS). In this nanoframework, CS endows CS/NPs with specific tumor-targeting activity and reduced systemic toxicity. Of note, the coordinated Zn^{2+} disrupts glycolytic processes and downregulates the expression of glucose transporter type 1 (GLUT1), thus depriving the cancer cells of their energy. Zn^{2+} further initiates the adenosine 5′-monophosphate activated protein kinase (AMPK) pathway, which leads to PD-L1 protein degradation and sensitizes CRC cells to immunotherapy. Moreover, the damaged double-stranded DNA during MTX treatment activates the cyclic GMP-AMP synthase-stimulator of interferon genes (cGAS-STING) pathway, which works together with TP5 induced the proliferation and differentiation of T lymphocytes and dendritic cells to further enhance the anti-CRC immune response. Therefore, CS/NPs efficiently sensitize cells to chemotherapy and stimulate systemic antitumor immune responses both in vitro and in vivo, representing a promising strategy to increase the feasibility of CRC immunotherapy.

Keywords Colorectal cancer, Immunotherapy, CGAS-STING pathway, Immune checkpoint blockade, Metal-organic nanoframework

†Xiaodian Zhang, Hailong Tian and Yang Chen contributed equally.

*Correspondence:
Na Xie
naxie@scu.edu.cn
Shaojiang Zheng
zshaojiang@muhn.edu.cn
Full list of author information is available at the end of the article

Graphical Abstract

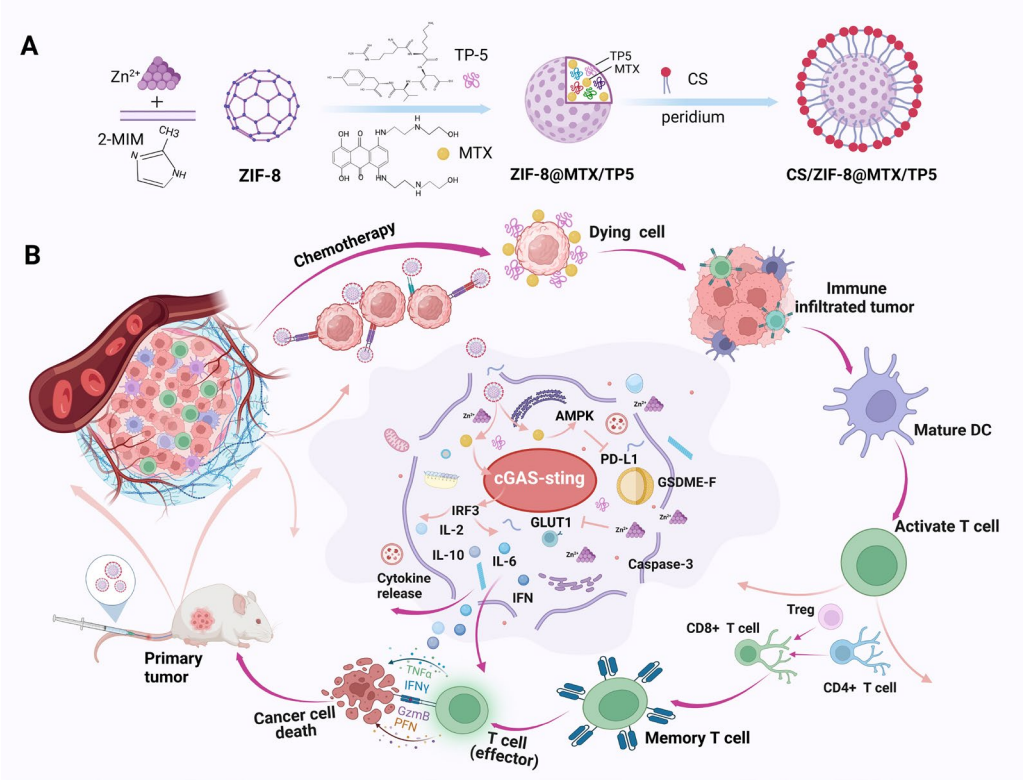

Introduction

Colorectal cancer (CRC), as the third most common cancer-related death cause [1, 2], is noteworthy for its high incidence rate and poor prognosis. Patients suffering from late-stage CRC have a five-year survival rate of only around 15% [3]. Cancer immunotherapy has shown marked progress in promoting systemic anti-CRC clinical effects [4, 5]. It has been reported that the activation of cGAS-STING signaling pathway is a key innate immune mechanism with great potential in CRC treatment [6, 7]. Upon activation, this pathway induces interferon (IFN) synthesis and initiates immunological responses in the tumor microenvironment (TME), leading to a strong anti-cancer immune response [8, 9]. Thus, stimulating the cGAS-STING pathway holds promise for CRC immunotherapy [10].

The clinical chemotherapeutic agent mitoxantrone (MTX) induces DNA damage in mitochondria and the nucleus by intercalating into DNA via hydrogen bonding [11–13]. The cGAS-STING pathway is activated by this process, causing the dendritic cells (DCs) to mature for effective antigen presentation, which further activates $CD8^+$ T cells to trigger an antitumor innate immune response [14, 15]. However, MTX has poor targeting and toxic side effects [16, 17]. Thymopentin (TP5) is an immunomodulatory pentapeptide (Arg-Lys-Asp-Val-Tyr, RKDVY) that has suitable biocompatibility and biodegradability for use in the clinic [18, 19]. TP5 plays a key role in cancer immunity through enhancing thymocyte differentiation and influencing the function of mature T-cells [20]. However, TP5 has high water solubility, possibly leading to a burst or uncontrolled release, and high loading levels are necessary to reach a sufficient TP5 dosage due to its half maximal inhibitory concentration (IC_{50}) [20]. Therefore, there is an urgent need to develop a suitable nanoplatform for the effective co-delivery of MTX and TP5.

The zeolitic imidazolate framework-8 (ZIF-8) is a Zn^{2+}-coordinated metal-organic framework (MOF) with the benefits of a high drug-loading capacity, targeted delivery, and pH-responsive release [21, 22]. Importantly, the coordinated Zn^{2+} can mediate the inhibition of glycolysis [23, 24] and the specific depletion of glucose transporter type 1 (GLUT1), thereby leading to the depletion of glucose within the cancer cells [25, 26]. The exhaustion of intracellular energy activates AMPK, a vital sensor of

bioenergetic equilibrium [27, 28]. AMPK promotes the phosphorylation of programmed cell death-ligand 1 (PD-L1) at the S195 site, causing the subsequent degradation of the PD-L1 protein [29, 30] and thereby decreasing expression levels of PD-L1 in tumor cells and suppressing cancer immune escape. As a result, in addition to providing a suitable drug delivery carrier, ZIF-8 has potential applications in preventing CRC immune escape and enhancing the immune response rate, thereby increasing the susceptibility of cancer cells to immunotherapy [31, 32].

Herein, we have engineered a pH-responsive ZIF-8 for the co-delivery of MTX and TP5 and used the tumor-targeting molecule chondroitin sulfate (CS) to obtain CS/ZIF-8@MTX/TP5 nanoparticles (CS/NPs). The engineered ZIF-8 is capable of site-specific delivery and efficient chemo-immunotherapy by activating the cGAS-STING pathway and inducing PD-L1 degradation. It has been reported that CRC cells highly express the CD44 receptor, which specifically recognizes and binds to glycosaminoglycan-based biomaterials such as chondroitin sulfate (CS) [33–35]. The attached CS, being a naturally occurring and biocompatible glycosaminoglycan, provides a hydrophilic and biocompatible surface to the nanoparticles, endows CS/NPs with specific tumor-targeting activity and reduced systemic toxicity [36, 37]. Of note, the coordinated Zn^{2+} disrupts glycolytic processes and downregulates the expression of GLUT1, which deprives the cancer cells of energy and further activates AMPK induces PD-L1 protein degradation, thus sensitizing cancer cells to immunotherapy. MTX-mediated treatment damages double-stranded DNA (dsDNA), activating the cGAS-STING pathway and further enhancing the anti-CRC immunity. In addition, Additionally, TP5 induces DCs and T lymphocytes to proliferate and differentiate, thereby amplifying the cancer-immunity cycle. CS/NPs can therefore efficiently sensitize cancer cells to chemotherapy while activate widespread antitumor immunity both in vitro as well as in vivo experiments, thereby offering an innovative potential CRC chemo-immunotherapy.

Experimental section

Materials

$Zn(NO_3)_2{\cdot}6H_2O$, sodium chondroitin sulfate, and 2,4-dimethylimidazolewere sourced from Shanghai Aladdin Biochemical Technology Co., Ltd. TP5 and MTX were provided by Meilun Biotech Co., Ltd. Thiazolyl blue tetrazolium bromide (MTT) was purchased from Aladdin Chemicals. The CT26 and RKO cells were provided by American Type Culture Collection (ATCC). DMEM/1640 culture medium was obtained from Gibco. FBS was purchased from BI. The Annexin V-FITC/PI and the TUNEL cell apoptosis detection and the cell apoptosis detection kits were provided by Yeasen Biotechnology Shanghai Co., Ltd. Enzyme-linked immunosorbent assay (ELISA) kits for mouse IL-2, mouse IL-6, mouse IL-10, mouse IFN-gamma (IFN-γ) and TNF-α were provided by ABclonal. The mouse granzyme B ELISA kit was purchased from Solarbio. Rabbit mAbs from Biolegend against the following were used: cGAS (79978), STING (13647), phospho-STING (AF7416), IRF-3 (4302 S), and phospho-IRF-3 (4302 S). Anti-GLUT1 rabbit mAb (bsm-52240R) was provided by Bioss Biotech Beijing Co. Ltd. (China). AMPK (ab72845), phospho-AMPK rabbit mAb (AP1002), β-actin rabbit mAb (AC050), and CD8A rabbit polyAb (A11856) were purchased from ABclonal. Anti-DFNA5/GSDME (ab215191) was provided by Abcam. PD-L1 rabbit mAb (M033179) was obtained from ABMART. Anti-caspase-3 (PTM-5752) and anti-cleaved-caspase-3 (PTM-77246) rabbit mAbs were purchased from Biolab. Ki67 rabbit polyAb (28074-1-AP) was provided by Proteintech. Anti-CD8 (GB114196) and Anti-CD4 (GB15064) antibodies were from Servicebio. The erythrocyte lysis buffer was provided by Beijing Solarbio. Beyotime provided the ATP detection kit.

Nanoparticle characterization

The Malvern Zetasizer Nano Analyzer was employed to detect the zeta potential and size distribution of different nanoparticles. Transmission electron microscopy (TEM) images were captured with an HT7800 TEM instrument (Hitachi, Japan). An ultraviolet-visible (UV-vis) spectrophotometer (UV-2700) was utilized to obtain the UV-vis spectra. A laser pointer (Senwei, China) was used to record the typical tyndall effect of nanoparticles. To conduct elemental analysis via X-ray photoelectron spectroscopy (XPS), a K-Alpha instrument obtained from Thermo Fisher Scientific was used, while data analysis was conducted through Avantage software from Thermo Fisher Scientific. The chemical structure of each samples was confirmed based on X-ray diffraction (XRD) by an X'Pert Pro MPD instrument and Fourier-transform infrared spectroscopy (FTIR) using a Thermo Fisher Scientific Nicolet iS5 instrument, both of which were integrated into the scientific compass platform (www.shiyanjia.com) for subsequent analysis. A microplate reader (Synergy H1, BioTek, Vermont, USA) was used to determine the ATP levels and cell viability. Fluorescence images, including images generated by EdU fluorescence labeling for cell proliferation, were acquired with an inverted fluorescence microscope produced by Olympus (Tokyo, Japan). The in-vivo biodistribution of CS/NPs was investigated with a small-animal imaging system (PerkinElmer, Massachusetts, USA). An automatic biochemical analyzer (Chemray 240, Rayto, China) was used to perform blood

biochemical analysis. The drug release data and ELISA measurements were obtained using a Tecan-Spark multifunctional microplate reader (Tecan, Switzerland). Cellular uptake, flow cytometry, and immunological analyses were completed with a BD FACSCelesta Analytical Flow Cytometer (BD/Becton Dickinson, New York New Jersey, USA).

Synthesis of ZIF-8@MTX/TP5

The synthesis of ZIF-8@MTX/TP5 NPs was accomplished following a one-pot method. First, to create solution A, both 40 mg MTX and 40 mg TP5 were dissolved in double-distilled water (ddH_2O, 4 mL). In parallel, 100 mg zinc nitrate $Zn(NO_3)_2{\cdot}6H_2O$ was dissolved in ddH_2O (0.4 mL) to obtain solution B, while 1 g 2-methylimidazole (2-MIM) was dissolved in ddH_2O (4 mL) to create solution C. Solution B was stirred at 600 rpm for 5 min, and solution A was then added dropwise while stirring for a further 10 min. The mixture was then added dropwise to solution C under continuous stirring at 800 rpm for 15 min. Subsequently, the product was obtained using centrifugation at 13,000 rpm for 30 min and rinsed three times in ddH_2O.

Synthesis of CS/ZIF-8@MTX/TP5

To synthesize CS/ZIF-8@MTX/TP5, of ZIF-8@MTX/TP5 nanoparticles (100 mg) were suspended in of 3% (w/v) chondroitin sulfate (CS) solution (30 mL). The suspension was subjected to probe sonication for 30 min, after which magnetic stirring proceeded at 1000 rpm for 24 h. After centrifugation, the product was washed three times with ddH_2O to obtain CS/NPs, as illustrated in Scheme 1A.

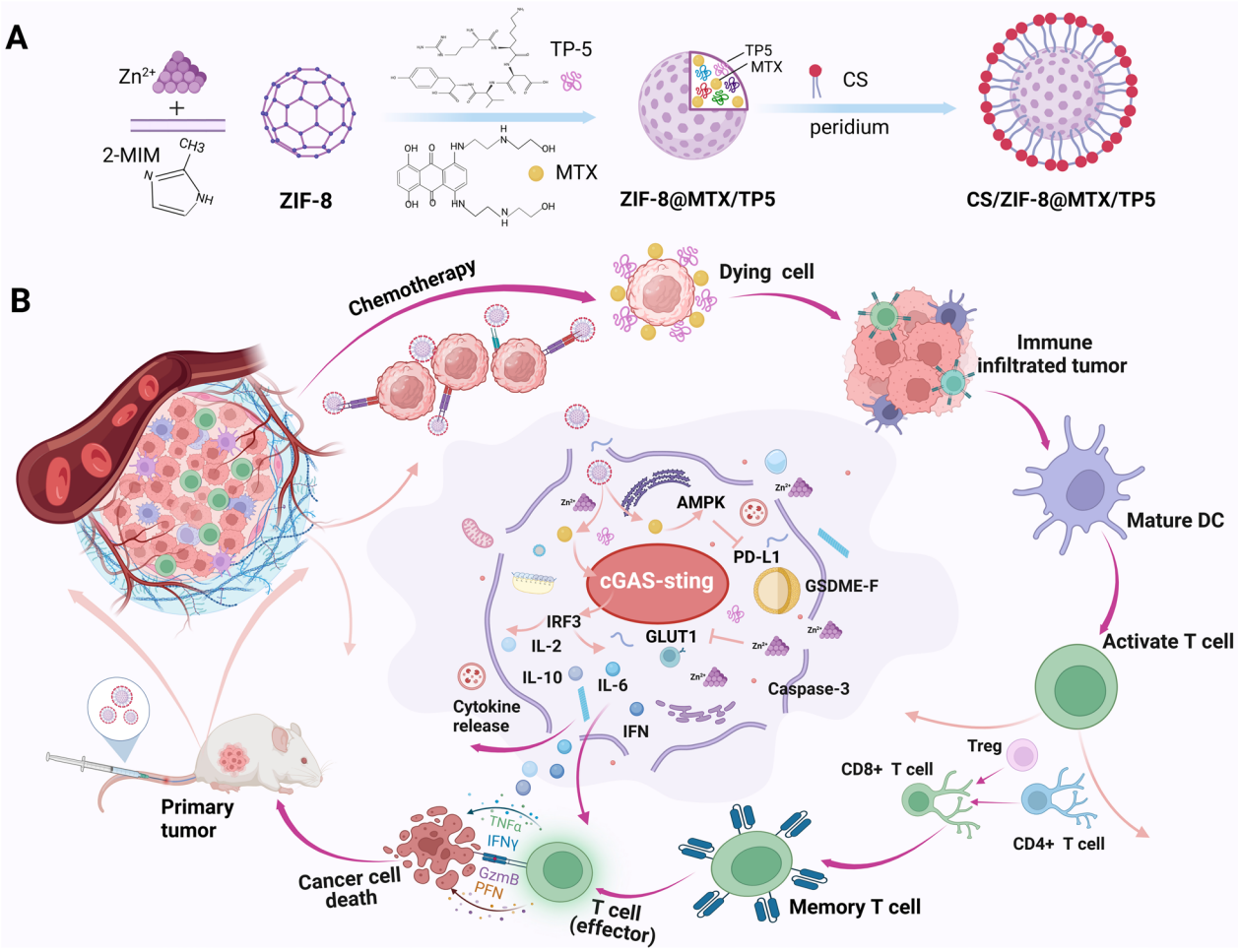

Scheme 1 **A** Synthesis of CS/ZIF-8@MTX/TP5 nanoparticles (CS/NPs). **B** Underlying mechanism of CS/NPs-mediated initiation of the cGAS-STING signaling pathway to promote synergistic chemo-immunotherapy

MTX and TP5 loading efficiency

The formula used to determine the loading efficiency of MTX and TP5 was as follows: Encapsulation efficiency (%) = $W_E/W_T \times 100$, where W_E is the quantity of MTX and TP5 encapsulated in CS/ZIF-8@MTX/TP5. W_T represents the entirety of MTX and TP5 added. The amounts of MTX and TP5 were determined through UV-vis spectroscopy absorption based on the standard curves.

Cell culture conditions

The mouse-derived CRC cell line CT26 and the human-derived CRC cell line RKO was conducted in RPMI 1640 medium (Gibco) by adding 1% penicillin-streptomycin and 10% FBS. Cell culture proceeded in an incubator maintained at 37 °C in a 5% CO_2 atmosphere.

Cellular uptake assay in vitro

To investigate the absorption of CS/NPs, RKO and CT26 cells were added to six-well plates (density: 2×10^4 cells/well). The culture medium was taken out, and the wells were provided with fresh medium containing 10 μM NPs. Cell incubation was then conducted for 0, 1, 2, 4, 6, and 8 h. Following incubation, cells were rinsed thrice in PBS for the removal of drug residue. The absorption was assessed via flow cytometry and inverted fluorescence microscopy to examine digested and fixed cells.

Cell viability assay

To assess the cytotoxicity of CS/NPs, an MTT assay was performed. RKO and CT26 cells were added to 96-well plates (density: 4×10^3 cells/well) and allowed to incubate overnight. After incubation, cells underwent 24 h of treatment with normal saline (Ctrl) and varying concentrations of drugs singly or in combination (TP5, MTX, MTX/TP5 (M + T), NPs, and CS/NPs). Supernatant collection and cell rinsing with PBS were conducted prior to the MTT assay using a microplate reader. In addition, the anti-proliferative ability of different treatments were further assessed using colony formation assays. Twenty-four-well plates were used for the assay, with RKO and CT26 cells seeded (density: 1×10^3 cells/well) and incubated for 3 days. After incubation, cells were subjected to treatments with Ctrl, TP5, MTX, (M + T), NPs, or CS/NPs. Following drug withdrawal, the cells were cultured in an incubator at 37 °C under a 5% CO_2 atmosphere for 7 days. The resulting cell colonies were gently rinsed three times, fixed for 30 min in 4% paraformaldehyde (PFA), and stained with crystal violet. The colony numbers were captured with a digital camera, and ImageJ software was employed to perform counting. The colony formation rate (%) was calculated based on comparing the area of crystal violet staining in different groups.

EdU labeling assay

EdU labeling was explored using the EdU Cell Proliferation Assay Kit. In brief, CRC cells were added to 96-well plates (density: 5×10^3 cells/well) and subjected to treatment with various concentrations of Ctrl, TP5, MTX, M + T, NPs, and CS/NPs based on the drug uptake times. Following the removal of the supernatant and incubation for a further 24 h, photographs of the cells were captured with an inverted fluorescence microscope and counted with ImageJ software.

Cell apoptosis assay

The Annexin V-FITC/PI Cell Apoptosis Assay Kit was utilized to determine the rate of tumor cell apoptosis. Six-well plates were used to incubate cells seeded (density: 5×10^4 cells/well) for 24 h. Subsequently, cells were subjected to treatment with Ctrl, TP5, MTX, M + T, NPs, or CS/NPs and incubated for a further 24 h. Cells were then stained with both annexin V-FITC and PI (30 min) following the manufacturer's protocol. Finally, flow cytometry was performed for the assessment of apoptosis in accordance with the manufacturer's instructions.

Western blotting

After drug treatment, cells were taken via scraping, rinsed using cold PBS, and subjected to sonication in radioimmunoprecipitation assay (RIPA) buffer containing SDS (0.1%), sodium deoxycholate (1%), and Triton X-100 (1%), with added phosphatase inhibitors and protease inhibitors. SDS-PAGE was performed on the lysates, which were then transferred onto PVDF membranes. Next, the membranes were blocked at room temperature for 2 h using skimmed milk. Incubation was carried out at 4 °C with specific primary antibodies followed by 2 h

(See figure on next page.)

Fig. 1 CS/NPs preparation and characterization. **A** Typical Tindall effects of ZIF-8, ZIF-8@MTX/TP5, and CS/ZIF-8@MTX/TP5. TEM photographs of **B** ZIF-8, **C** NPs, and **D** CS/NPs. Scale: 100 nm. **E** Zeta potential measurements for ZIF-8, NPs, and CS/NPs nanoparticle ($n = 3$). **F** CS/NPs particle size distribution following 180 days of storage and TEM images following 6 months of storage. **G** UV-vis absorption spectra of MTX, M + T, NPs, and CS/NPs. **H** XRD patterns of ZIF-8, NPs, and CS/NPs. **I** Corresponding elemental mapping (XPS spectra) of Zn, C, S, and N signals. **J** FTIR spectra of ZIF-8, NPs, and CS/NPs. **K** Release behavior of MTX at pH 7.4 and 5.0 ($n = 3$). **L** Release behavior of TP5 at pH 7.4 and 5.0 ($n = 3$)

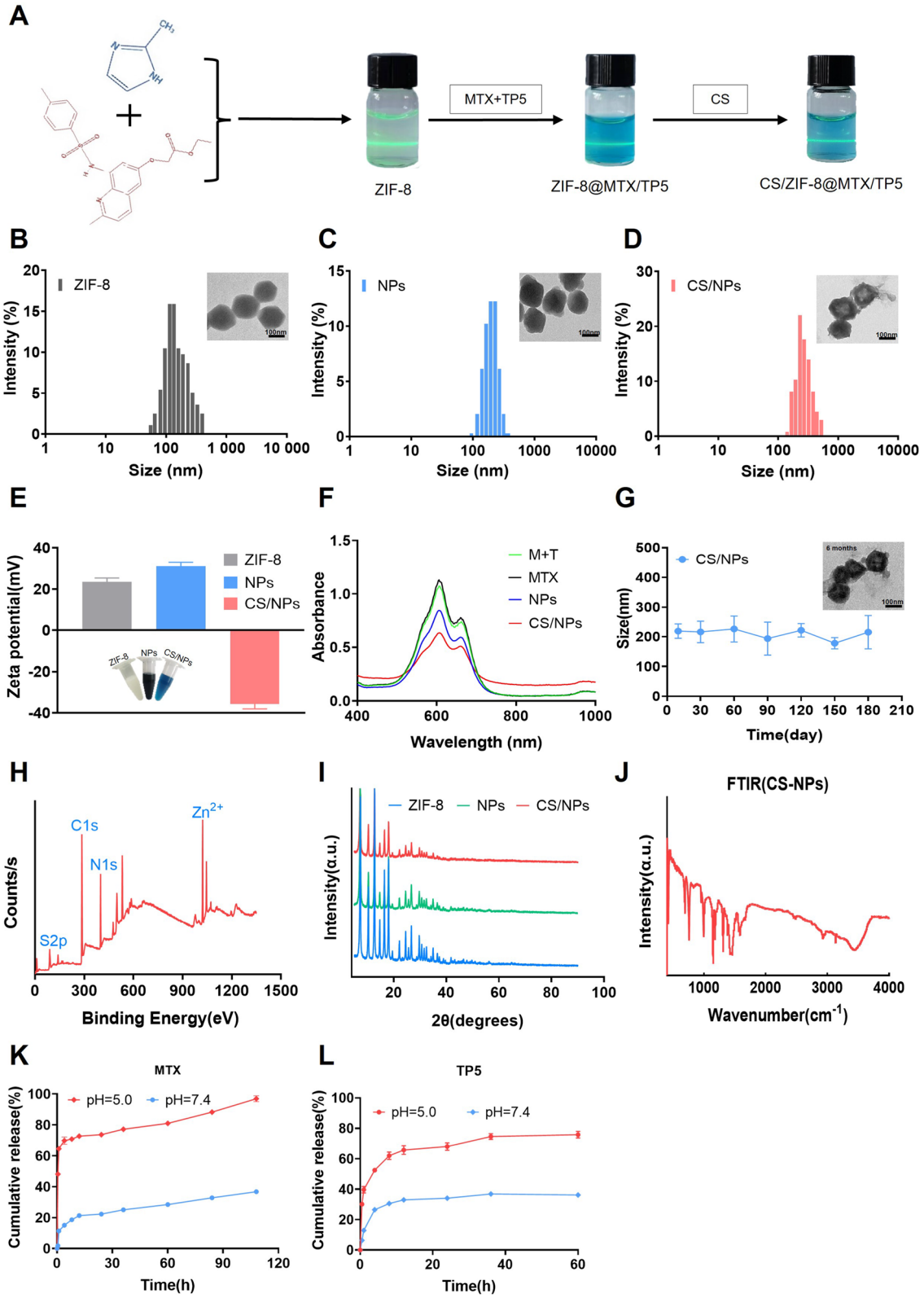

Fig. 1 (See legend on previous page.)

incubation with secondary antibodies. Protein expression was visualized using Immobilon Western HRP Substrate and the ChemiScope 0050 Touch Integrated Chemiluminescence Imaging System.

ATP detection assay

ATP detection kits were employed to determine the level of ATP. In this assay, cells were seeded in six-well plates (density: 96×10^4 cells/well). After drug intervention, the cell culture supernatant was collected and processed. Then, 20 μL supernatant was mixed with a portion of the assay's working solution (100 μL). A multifunctional enzyme marker was used to obtain the ATP fluorescence intensity.

Co-culture experiments

We validated the in vitro liposomal cell immunological results through co-culture experiments. Cell culture was performed in six-well plates (density: 5×10^4 cells/well). Following drug treatment, the cells underwent incubation for 24 h. Additionally, splenic cells were obtained from female BALB/c mice and seeded in the six-well plates. Co-incubation of tumor cells and splenic cells was conducted in an incubator at 37 °C for 48 h. The supernatant containing the cells was harvested and underwent centrifugation at 4000 rpm for 3 min. Following centrifugation, the supernatant was disposed of and the cells were obtained. The cells in the six-well plates were treated with trypsin and the digestion was terminated with a complete culture medium. Following centrifugation at 4000 rpm for 3 min, the supernatant was discarded and the cells were collected. The cells underwent staining with anti-CD11c-PE, anti-CD80-FITC, anti-CD86-APC, anti-CD3-FITC, anti-CD4-PE, and anti-CD8-APC antibodies, and flow cytometry was employed to determine the percentage of mature DCs and T-cell activation.

In vivo imaging and biodistribution analysis

To assess drug accumulation in the tumor area, the drugs were intravenously administered to Luc-CT26 subcutaneous tumor-bearing mice when the tumor volume reached 150–200 mm^3. First, free single-drug MTX (1 mg kg^{-1}), non-targeted ZIF-8@MTX/TP5 (2 mg kg^{-1}), and CS/ZIF-8@MTX/TP5 (2 mg kg^{-1}) were injected into the tail vein. Mice underwent anesthesia with 3% isoflurane, and images of mice were captured with an in-vivo imaging system (IVIS Lumina XR III, PerkinElmer, Massaachusetts, USA) at 1, 2, 4, 6, 8, and 24 h post-injection. Mice were euthanized for biodistribution analysis following the 24-h imaging, and tumors and major organs were dissected and used to obtain ex-vivo fluorescence images.

In vivo antitumor study

Yaokang Biotechnology Co., Ltd. (Chengdu, China) supplied six-week-old female BALB/c mice that weighed approximately 18–20 g. All the animals studies were conducted in accordance with the "Guidelines for Animal Experiments" and were approved by the Sichuan University Animal Ethics and Use Committee. First, a unilateral subcutaneous tumor model was created through the injection of mice with Luc-CT26 colorectal cancer cells (5.0×10^5 cells suspended in serum-free 1640 medium) in the right axillary subcutaneous region. When the volume of the tumors had grown to 100 mm^3, mice were selected at random and split into six groups ($n=5$ per group) to explore the antitumor effects of the multifunctional NPs. All drug treatments, namely, Ctrl (normal saline), TP5, MTX, (M+T), NPs, and CS/NPs (2 mg/kg), were administered to mice by tail vein injection every other day. The tumor volume and body weight of mice were recorded every 2 days. A vernier caliper was used to obtain the tumor size, and the volume of tumors (mm^3) was determined by the following formula: $\text{Tumor Volume}\left(mm^3\right)=\frac{\text{Length}\times\text{Width}^2}{2}$. On day 15 of therapeutic intervention, all mice were euthanized and tumor tissue were removed and weighed to assess the antitumor effect of drug treatments. The tumor inhibition rate was calculated according to the following equation:

$$\text{Inhibition Rate (\%)}\frac{\text{Tumor weight in control group}-\text{Tumor weight in treatment group}}{\text{Tumor weight in control group}}\times\ 100\%.$$

(See figure on next page.)

Fig. 2 CS/NPs uptake and cytotoxicity. **A**, **B** Representative flow cytometry images depicting CT26 and RKO cell uptake following incubation with CS/NPs at different points in the experiment. **C**, **D** Flow cytometry images of uptake by CT26 and RKO cells after different treatments. **E**, **F** Viability of CT26 and RKO cells treated with different samples ($n=3$). **G**–**J** Assessment of colony formation and quantitative metrics in CT26 and RKO cell. **K**–**N** Fluorescence imaging and quantitative analysis of EdU labeling experiments in CT26 and RKO cells following various treatments. **O**–**R** Apoptosis in CT26 and RKO cells treated with different samples ($n=3$). ***$p<0.001$

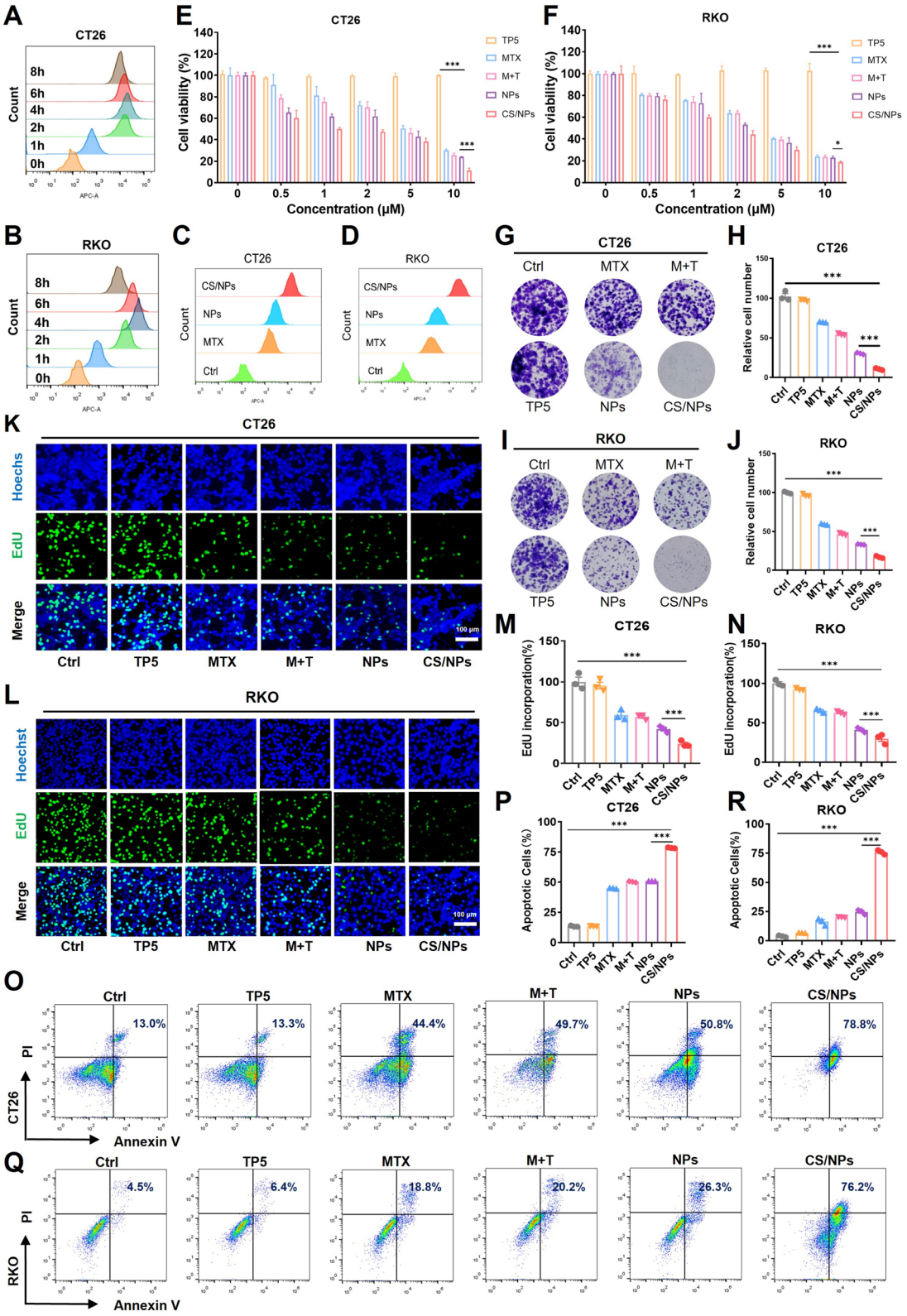

Fig. 2 (See legend on previous page.)

The tumors and spleen, heart, kidneys, liver, lung tissue were further harvested for subsequent experiments.

Anti-tumor immune activation experiment

Tumor tissue and spleens were collected from the treated mice at the 15th day, and grinding and processing were used to prepare single-cell suspensions. Cell staining was conducted using anti-CD11c-PE, anti-CD3-FITC, anti-CD4-APC, anti-CD80-FITC, anti-CD4-PE, anti-CD86-APC, anti-CD8-APC anti-CD25-FITC, and anti-Foxp3-PE antibodies, after which flow cytometry was performed.

The activation of immune response

In this study, a bilateral subcutaneous tumor model was established using BALB/c mice through the intratumoral injection of CT26-Luc cells (5×10^5 cells) to induce the growth of proximal primary tumors in the left axillary subcutaneous region of female BALB/c mice coupled with the subcutaneous injection of CT26-Luc cells (5×10^5 cells) into the right axillary subcutaneous region of the same mouse to induce the growth of distal tumors. When the volume of tumors had grown to approximately 6 mm, mice were selected at random and placed into one of six groups: Ctrl (control), TP5, MTX, (M + T), NPs, and CS/NPs ($n=5$ per group). Peritumoral drug administration was conducted on alternating days, with the tumor volume and body weight of each mouse recorded every 2 days. On day 14, bilateral tumor tissues and spleens were excised from treated mice and processed to generate single-cell suspensions. Tumor cells underwent staining with anti-CD11c-FITC, anti-CD80-APC, anti-CD86-PE, anti-CD3-FITC, anti-CD4-PE, anti-CD8-APC, anti-CD4-APC, anti-CD25-FITC, and anti-Foxp3-PE antibodies, after which flow cytometry was performed to obtain the proportions and numbers of $CD4^+$ and $CD8^+$ T cells in the proximal left and distal right tumors and spleens.

Histological staining

The harvested mouse tumors and major organs were fixed using 4% PFA and then embedded in paraffin. Tissue sections with a thickness of 4 μm were taken from paraffin-embedded blocks and histological examination was performed based on hematoxylin and eosin (H&E) staining. In addition, immunohistochemical staining (IHC) was conducted for KI67, PD-L1, cGAS, and P-STING to evaluate protein expression levels in tumor tissues.

Immunofluorescence

First, cells were placed onto glass coverslips in 24-well plates (density: 5×10^3 cells/well) and left to adhere for 24 h. After 24 h, the cells were fixed in 4% PFA, rinsed using PBS, and permeabilized with 0.4% Triton X-100. The cells were then blocked with 5% FBS and incubated with primary antibodies specific for CD4 and CD8. Following incubation with primary antibodies, the cells underwent treatment with CY3-labeled goat anti-rabbit IgG secondary antibodies. Cellular images were captured using a scanner (Pannoramic MIDI, 3DHISTECH, Hungary).

ELISA assays

ELISA assays were conducted using specific ELISA kits. Mouse sera were collected, and the concentrations of cytokines including TNF-α, IFN-γ, IL-1, IL-2, IL-6, IL-10, and granzyme B were determined using the respective ELISA kits. Concentration measurements were analyzed using the Tecan-Spark Multimode Microplate Reader.

Serum biochemical analysis

Biochemical assay kits were employed to analyze the mouse sera. The concentration of aspartate aminotransferase (AST), alanine aminotransferase (ALT), creatinine (CRE), and urea, which serve as markers of kidney and liver function, were determined with an automated biochemical analyzer.

Statistical analysis

We used GraphPad Prism 8.0 software for statistical analyses, which were performed using one-way analysis of variance (ANOVA) or t-tests. The related data were shown as the Mean ± Standard Deviation (SD) of at least 3 separate assays. *mean $p<0.05$; ** mean $p<0.01$; *** mean $p<0.001$; NS mean not significant.

(See figure on next page.)

Fig. 3 CS/NPs-mediated in-vitro immune activation. **A** CS/NPs molecular mechanism illustrated in a schematic. **B** Western blotting results for cGAS, STING, P-STING, IRF-3, and P-IRF-3. **C** Western blotting results for GLUT1, AMPK, phosphorylated AMPK, and PD-L1. **D**, **E** Characteristic flow cytometry visuals showing depicting mature DCs ($CD80^+/CD86^+$ cells gated within $CD11c^+$ cells) and activated T lymphocytes cells ($CD4^+/CD8^+$). **F**, **G** Quantitative analysis of mature DCs ($CD80^+/CD86^+$ cells gated within $CD11c^+$ cells) and activated T lymphocytes cells ($CD4^+/CD8^+$), ($n=3$). **H** Western blotting results for cleaved-caspase-3, caspase-3, and GSDME-F. **I**, **J** Depletion of ATP in intracellular and extracellular spaces ($n=3$). ***$p<0.001$

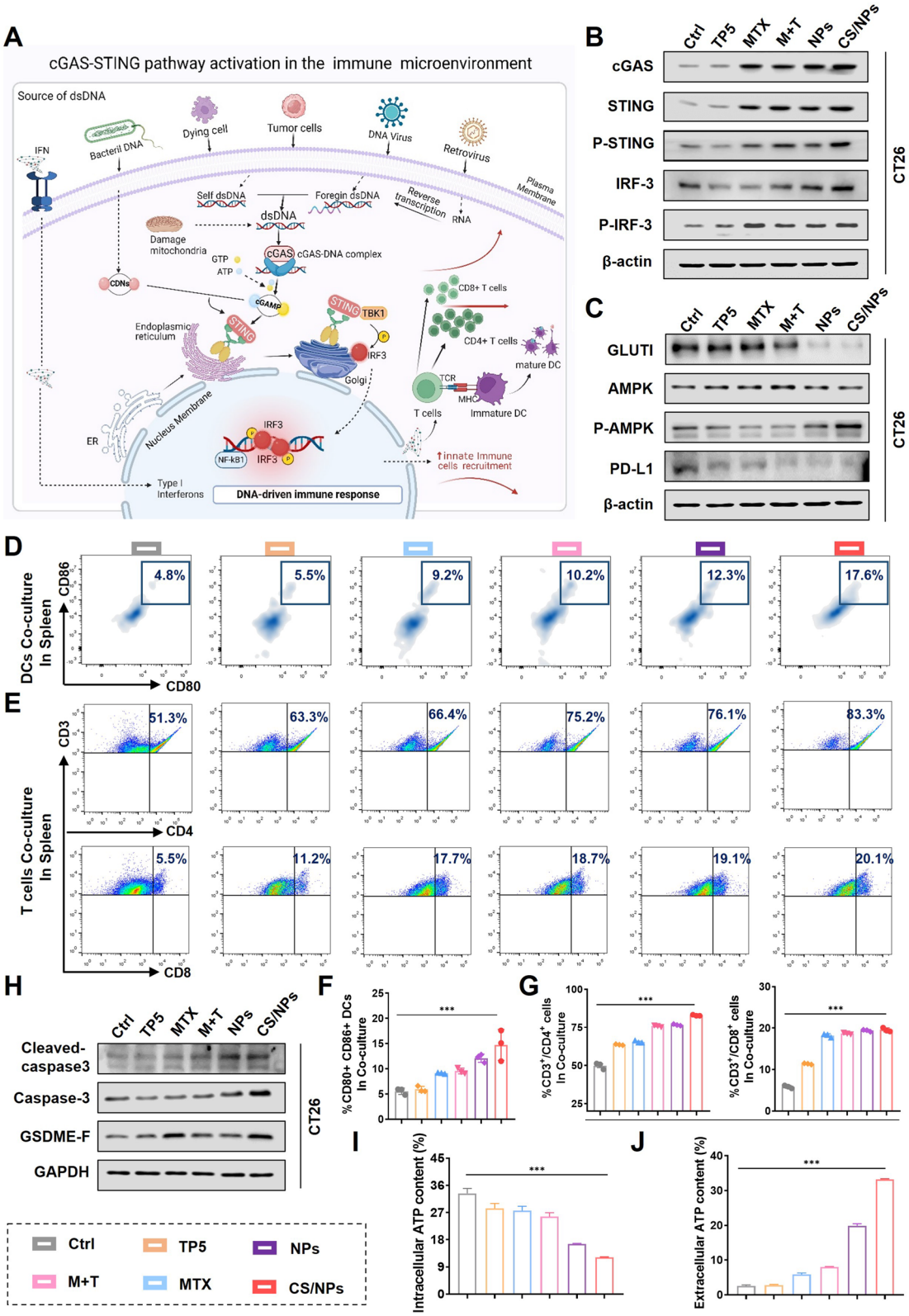

Fig. 3 (See legend on previous page.)

Results and discussions

Preparation and characterization of CS/NPs

CS-tailored ZIF-8@MTX/TP5 nanoparticles were prepared using a one-pot synthetic method. The protocol for the preparation of CS/NPs was shown in Fig. 1A. Images obtained using TEM revealed a shift in morphology between NPs and CS/NPs from an orthohexagonal to a spherical shape, illustrating the functionlization of CS on the surface of the NPs (Fig. 1B–D). Based on dynamic light scattering, the average size of ZIF-8, NPs, and CS/NPs were 167.0, 224.8, and 278 nm, respectively, which was in accordance with the TEM images (Fig. 1B–D) and showed that they were suitable for tumor accumulation owing to the enhanced permeability and retention effect. Following CS modification, the CS/NPs had a zeta potential of about − 36 mV, which hindered the aggregation of CS/NPs in aqueous solutions (Fig. 1E). The UV-vis spectra indicated that the CS/NPs had a maximum absorption wavelength of 606 nm, implying the successful loading of free MTX (Fig. 1F). Additionally, no fluctuations in particle size or morphology were observed over 6 months (Fig. 1G), demonstrating satisfactory storage stability after the therapeutic agents were packaged into the prepared CS/NPs.

The XRD spectra confirmed the stability of the CS/NPs structure. The characteristic diffraction peak positions of the CS/NPs samples remained unchanged, matching well with the ZIF-8 single crystal structure, and the peaks were sharp, indicating good crystallinity of the final product (Fig. 1H). XPS-based elemental analysis (Fig. 1I) revealed that C, N, S, and Zn^{2+} were distributed throughout the CS/NPs, indicating that they were well encapsulated in the ZIF-8 NPs. Furthermore, the characteristic absorption peak of carbohydrate in 2900 cm^{-1} and the presence of sulfuric acid group near 1240 cm^{-1} indicated that CS was successfully modified on the surface of the ZIF-8 NPs (Fig. 1J). To study the loading capacity of ZIF-8 using UV-Vis spectrophotometry, standard curves of MTX and TP5 were constructed. The MTX and TP5 loading efficiencies were calculated as 19.0% and 13.0%, respectively. The release behavior of MTX or TP5 from the nanoparticles was then determined after incubation for 48 h at 37 °C. MTX in CS/NPs exhibited release rates of 51.4% and 73.5% at pH 7.4 and pH 5.0, respectively (Fig. 1K). TP5 in CS/NPs exhibited release rates of 36.2% and 75.8% at pH 7.4 and pH 5.0, respectively (Fig. 1L). It should be noted that MTX and TP5 were effectively released from CS/NPs in CRC sites under acidic conditions. Therefore, the coating of CS on the surface of ZIF-8 NPs did not affect the release of the loaded drugs MTX and TP5.

CS/NPs cellular uptake and cytotoxicity

To effectively treat tumors, endocytosis is crucial for drug accumulation in cells [38]. To determine the appropriate time for treating tumor cells with drugs, the uptake behavior of CS/NPs was evaluated in CRC cell lines (CT26 and RKO) at 0, 1, 2, 4, 6, and 8 h using fluorescence microscopy and flow cytometry. As illustrated in Fig. 2A–B and S1A–B (Supporting Information), CS/NPs exhibited optimal drug uptake and internalization, achieving peak levels at 4 h. Additionally, we studied the internalization efficiency of CS/NPs, Ctrl, free MTX, and non-targeted NPs in CT26 and RKO cells after 4 h of incubation (Fig. 2C–D and Figure S1C–D, Supporting Information). NPs exhibited significantly higher fluorescence than free MTX, indicating that the endocytosis mediated by the NPs was more efficient than free diffusion. CS/NPs showed higher cellular internalization efficiency in cancer cells compared to non-targeted NPs, indicating that CS-mediated endocytosis significantly improved the targeting efficiency of CS/NPs. Subsequently, Using the MTT test, we evaluated the cytotoxicity of CS/NPs. In comparison with the other groups, CS/NPs exhibited higher tumor-inhibiting capabilities at equimolar doses (Fig. 2E–F). Additionally, the anti-proliferative ability of the CS/NPs was measured in colony formation assays (Fig. 2G–J) and EdU staining experiments (Fig. 2K–N) and the results were consistent with the MTT assay results. Previous research has shown that free MTX has pro-apoptotic effects [39, 40]. Flow cytometry results and quantitative analysis of CRC cell lines CT26 and RKO (Fig. 2O–P and Q–R) showed that CS/NPs had stronger pro-apoptotic abilities compared to free MTX and non-targeted NPs, suggesting they have great potential for CRC treatment.

(See figure on next page.)

Fig. 4 CS/NPs biodistribution and anti-tumor efficacy in-vivo. **A** Quantitative analysis and real-time fluorescence imaging in-vivo of the CT26-Luc subcutaneous tumor model. **B** Fluorescence intensity analysis ex vivo in primary organs and tumor tissues. **C** Schematic illustration of in-vivo drug treatment in the unilateral mouse tumor model. **D** Body weight modifications across six mouse cohorts under different drug treatments ($n = 5$). **E** Comparison of tumor volume curves ($n = 5$). **F**–**K** Tumor volume change curves ($n = 5$). **L** Corresponding tumor photographs, scale bar: 1 cm ($n = 5$). **M** Average tumor weight and inhibition rate ($n = 5$). **N** Images depicting tumor tissues collected from various groups subjected to Ki67 immunohistochemistry, and H&E staining. With a Scale bar: 50 μm. ***$p < 0.001$

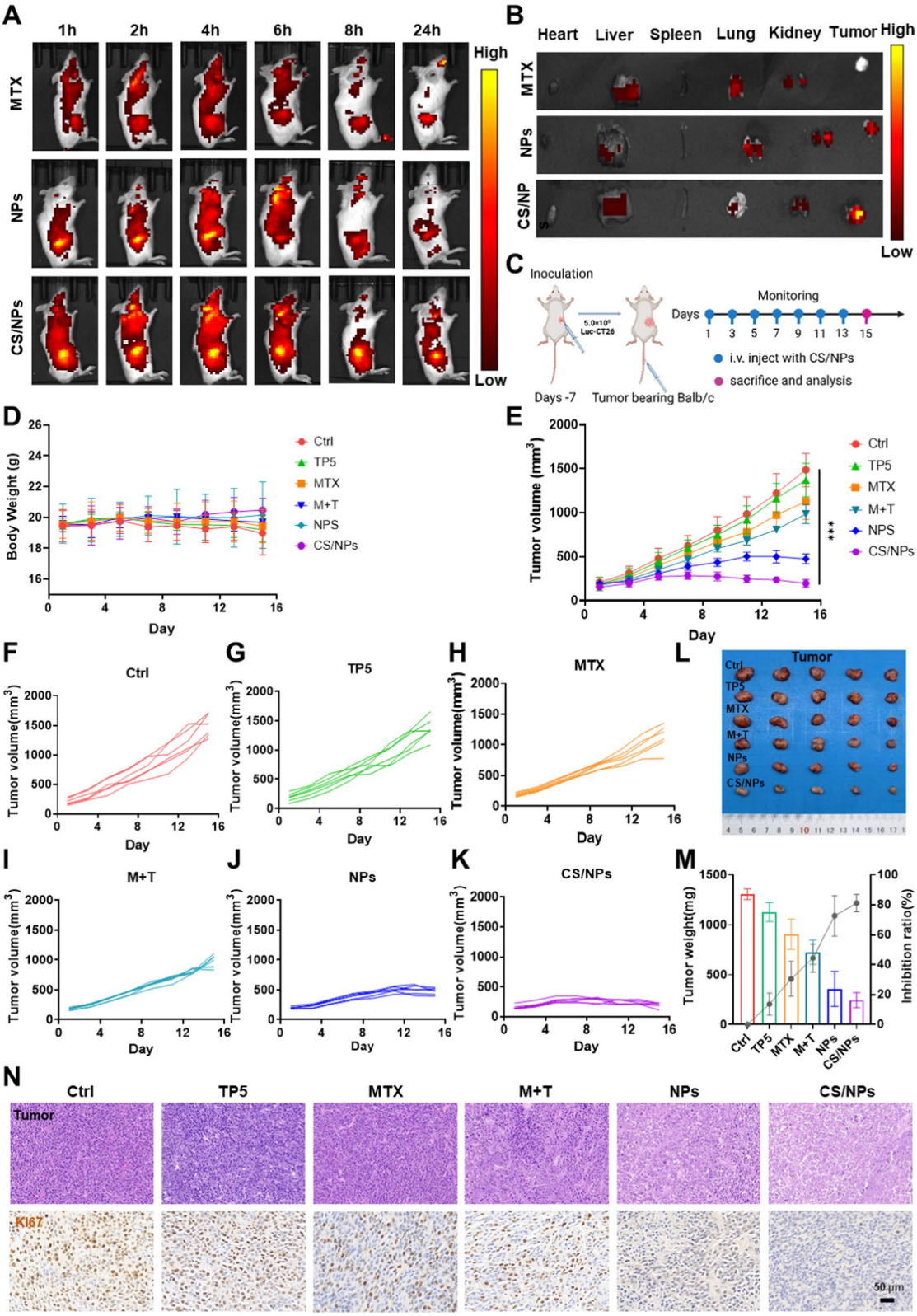

Fig. 4 (See legend on previous page.)

CS/NPs regulate cGAS-STING-mediated in vitro immune activation

We have verified that the CS/NPs demonstrate robust antitumor capabilities in in vitro experiments with CRC cells. Increasing amounts of evidence show that the stimulation of cGAS-STING signaling is considered a potential therapeutic approach for enhancing antitumor immune responses [41, 42]. This approach can recruitment and activate TBK1, which in turn activates IRF3, inducing the secretion of type I interferon (IFNs, particularly IFN-β) to initiate innate immunity [43, 44]. The findings of this research demonstrate that the free chemotherapy drug MTX Facilitates activation of cGAS-STING signalingpromotes the activation of the cGAS-STING signaling pathway via increasing the sensitivity of cGAS to cytoplasmic tumor dsDNA, causing dendritic cell maturation and activating $CD8^+$ T cells (Fig. 3A). Western blot analysis assessed protein expression linked to the cGAS-STING pathway. As illustrated in Fig. 3B and Figure S2I (Supporting Information), the phosphorylation levels of cGAS, STING, and IRF3 in the CS/NPs-treated group showed significant upregulation in comparison to free MTX, implying that CS/NPs enhanced cGAS-STING pathway activation. Quantitative analysis of relative protein expression in Figure S2A–C and Figure S2K–M (Supporting Information). A subsequent study examined GLUT1, AMPK, and PD-L1 protein expression levels (Fig. 3C and Figure S2J, Supporting Information). CS/NPs treatment decreased the expression of GLUT1 and PD-L1 while promoting the phosphorylation of AMPK. Quantitative analysis of relative protein expression in Figure S2D–F and Figure S2N–P (Supporting Information).

Furthermore, we seted up a co-culture assay to delineate the immunomodulatory effects of CS/NPs. Using flow cytometry images and quantitative analysis in co-cultured CT26 cells, we assessed the proportion of mature DCs and activated T cells following drug intervention. CS/NPs treatment enhanced the maturation of DCs in CT26 cells in comparison with the control and NPs treatments, with significantly upregulated expression of the co-stimulatory molecules CD80 and/or CD86 (gated by $CD11c^+$ DCs; Fig. 3D, F). Additionally, T cells with $CD4^+/CD8^+$ activation were significantly more active (Fig. 3E, G).

Markers of pyroptosis, including cleaved-caspase3, caspase-3, and GSDME-F (a key effector of burnout) proteins, were significantly upregulated after treatment with CS/NPs (Fig. 3H), suggesting that the coordinated Zn in the ZIF-8 played an important role in CRC treatment. Quantitative analysis of relative protein expression in Figure S2J–H (Supporting Information). This study then used the ATP assay kit to determine the intracellular ATP concentrations of CRC cells following different. Experimental outcomes indicated that CS/NPs significantly decreased intracellular ATP levels (Fig. 3I) while significantly increasing extracellular ATP levels (Fig. 3J), indicating that the coordinated Zn in the ZIF-8 treatment had a pronounced inhibitory effect on ATP production. The above findings indicate that CS/NPs promote the cGAS-STING pathway in vitro, induce DC maturation, and activate T cells.

CS/NPs biodistribution and antitumor effectiveness in vivo

The tumor-specific targeting ability by CS/NPs is a critical property for in vivo antitumor efficiency. A subcutaneous BALB/c mouse tumor model representative of in vivo biodistribution was constructed (Figure S3A, Supporting Information). In the tumor, the CS/NPs accumulation was greater than that of free MTX and non-targeted NPs at all time points (Fig. 4A). Mice were euthanized following the real-time monitoring of drug treatment and all major organs and neoplastic tissues were harvested to conduct fluorescence imaging and quantitative analysis in an ex-vivo (Fig. 4B). Compared to free MTX and non-targeted NPs, the fluorescence of CS/NPs in tumor tissues was greater and lasted longer than in the other groups.

Next, we established a CT26-Luc unilateral subcutaneous tumor model in BALB/c mice. In each group, an equivalent of 2 mg kg^{-1} MTX was administered through tail vein injection every other day for 15 days (Fig. 4C). We monitored tumor volume and body weight of mice on alternating days along the entire treatment process. Compared to the control, body weights in tumor-bearing mice within the teratment groups had no significant

(See figure on next page.)

Fig. 5 Activation of cGAS-STING by CS/NPs enhances the in vivo immune response. **A** Flow cytometry results for mature DCs in mouse tumor tissue, including $CD11c^+$ gated $CD80^+$ $CD86^+$. **B** Flow cytometry results for Treg cells in mouse tumor tissue after different treatments. **C** Percentage of mature DCs in mouse spleens, gated by $CD80^+$ $CD86^+$, after various treatments. **D**, **E** Proportions of T cells in mouse tumor tissue following different treatments, including $CD3^+$-gated $CD4^+$ and $CD8^+$ T cells. **F** Percentage of Treg cells in mouse tumor tissue after different treatments. **G** Immunohistochemical analysis of cGAS, PD-L1, and STING. Scale bar: 50 μm. **H** Immunofluorescence staining of $CD8^+$ and $CD4^+$ T cells within tumor specimens. Scale bar: 100 μm. **I**–**N** Concentration of cytokines (pg/mL) in mouse serum, such as IFN-γ, TNF-α, granzyme B, IL-10, IL-2 and IL-6, were assessed using ELISA kits. $^{**}p < 0.01$; $^{***}p < 0.001$

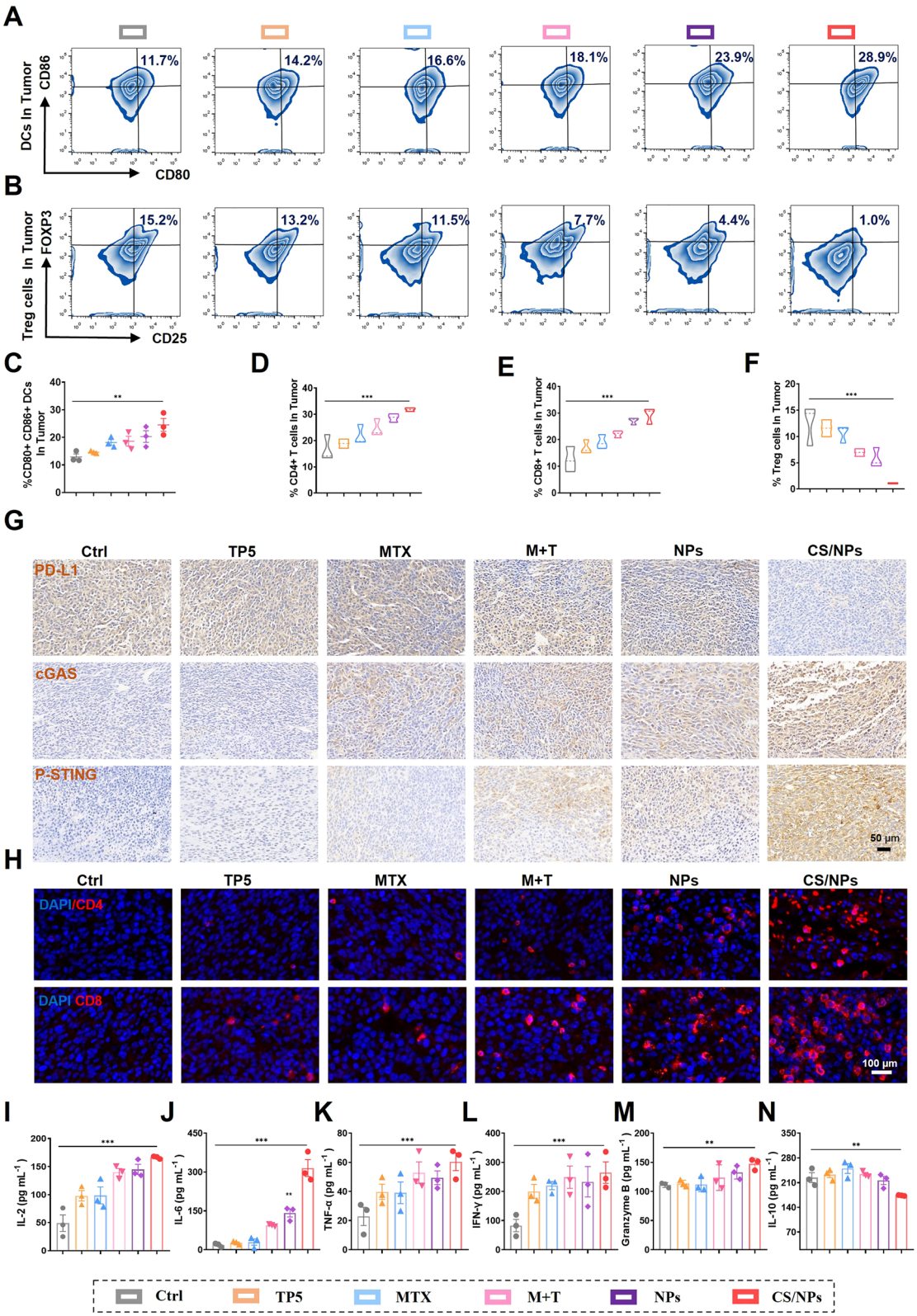

Fig. 5 (See legend on previous page.)

fluctuations (Fig. 4D). Tumor volume plots were created for all six groups of mice (Fig. 4E) and for each group individually (Fig. 4F–K). The plots showed that, compared to the control, mice subjected to treatment with MTX alone (Day 15 ≈ 1357 mm^3) showed scarce differences in terms of in tumor growth, which may have been due to the low dose (1 mg kg^{-1}) and limited circulation in tumor tissues. However, tumor growth in mice exposed to CS/NPs was remarkably inhibited. The CS/NPs-treated group achieved the most effective tumor growth suppression on day 15 of treatment, with tumors growing to only around 200 mm^3, consistent with the cytotoxicity results. When treatment concluded, the treated mice were euthanized and tumors were extracted, anatomized, imaged, and weighed (Fig. 4L). Images of tumors and the corresponding weights of tumors harvested from dissected mice visually illustrated that each treatment group showed some antitumor effectiveness, with CS/NPs having the strongest antitumor effect. CS/NPs treatment resulted in the smallest tumors, achieving an effective tumor growth inhibition rate of 89.1% (Fig. 4M). In addition, as shown in Fig. 4N, H&E staining of tumor slices from CS/NPs-treated mice revealed significant damage and necrosis of the tumor cells. Immunohistochemistry staining for Ki67 confirmed significant inhibition in the CS/NPs treatment group. The major organs underwent histological examination, revealing no significant morphological alterations in the CS/NPs-treated group (Figure S3B, Supporting Information). This finding supported the promising biocompatibility of this drug delivery approach.

Activation of cGAS-STING enhances the immune reaction elicited by CS/NPs in vivo

The in-vitro co-culture experiments indicate that CS/NPs are able to effectively induce an immune response in-vitro. This presents a critical point for cancer therapy. Based on these findings, we further explored whether CS/NPs could induce an antitumor immune response in vivo. Tumors were treated with different treatments and after treatment, the spleen and tumor tissues were collected from euthanized mice for flow cytometry to assess DC cell maturation, T-cell activation, and regulatory T cells (Treg cells) suppression. This study quantified the percentages of various T-cell populations, namely, $CD4^+$ helper cells, $CD8^+$ cytotoxic cells, and Treg cells.

As illustrated in Fig. 5A and C, treatment with CS/NPs increased the occurrence of DCs in the tumor tissue, which was in accordance with the findings of the in-vitro co-culture experiments. In previous studies, antigen-specific T-cell ($CD4^+$/$CD8^+$) infiltrating and activating in the TME has the ability to significantly enhance tumor suppression via promoting intercellular immune responses [45]. Therefore, this study examined tumor tissues to investigate the infiltration and activation of $CD4^+$/$CD8^+$ T cells. As shown in Fig. 5D–E and Figure S4A (Supporting Information), the CS/NPs treatment groups demonstrated increased T-cell ($CD4^+$ /$CD8^+$) infiltrations compared to other treatments. Additionally, the IHC results showed a significant downregulation of PD-L1 in the CS/NPs-treated group (Fig. 5G), which further lowered the level of Treg cells in the tumor to 1% (Fig. 5B). Studies have shown that in the malignant tumor microenvironment, Treg is also a key factor in mediating immune escape and thus promoting tumor progression, leading to tumor immunotherapy resistance and even disease hyperprogression [46, 47]. This suggests that CS/NPs may potentially overcome Treg cell-mediated immune escape, thereby improving the antitumor immune response. Furthermore, this study used IHC staining to examine cGAS and phosphorylated-STING-related proteins in tumor tissue slices collected from mice following treatment (Fig. 5G). CS/NPs-treated mice showed higher expression levels of cGAS and STING than mice in the control. As illustrated in Fig. 5C–F, quantitative analysis confirmed that treatment with CS/NPs both enhanced dendritic cell maturation and promoted the activation of $CD4^+$/$CD8^+$ T cells, aligning with immunofluorescence staining results (Fig. 5I). CS/NPs treatment simultaneously decreased the amount of Treg cells in the tumor tissue.

In comparison to the other groups, the group treated with CS/NPs showed a greater T-cell percentage ($CD4^+$/$CD8^+$), effectively promoting the production of more T cells in the spleen in addition to the activation of $CD4^+$/$CD8^+$ T cells (Figure S4B and S4E–G, Supporting Information). The maturation of DCs in the spleen (Figure S4C and Figure S4H, Supporting Information) was further

(See figure on next page.)

Fig. 6 CS/NPs induce cGAS-STING-mediated enhancement of distant tumor immunity. **A** Schematic representation of treatment for a bilateral subcutaneous Luc-CT26 tumor bearing model. **B** Corresponding primary tumor photographs, scale bar: 1 cm. **C** Comparison of primary tumor volume curves for the six groups during different drug treatments ($n = 5$). **D** Average tumor weights and inhibition rates ($n = 5$). **E** Corresponding distant tumor photographs, scale bar: 1 cm ($n = 5$). **F** Tumor volume curves ($n = 5$). **G** Average tumor weights and inhibition rates ($n = 5$). **H** H&E and immunohistochemical Ki67 staining In primary tumor tissue for each group, scale bar: 50 μm. **I** H&E and immunohistochemical Ki67 staining in distant tumor tissue, scale bar: 50 μm. ***$p < 0.001$

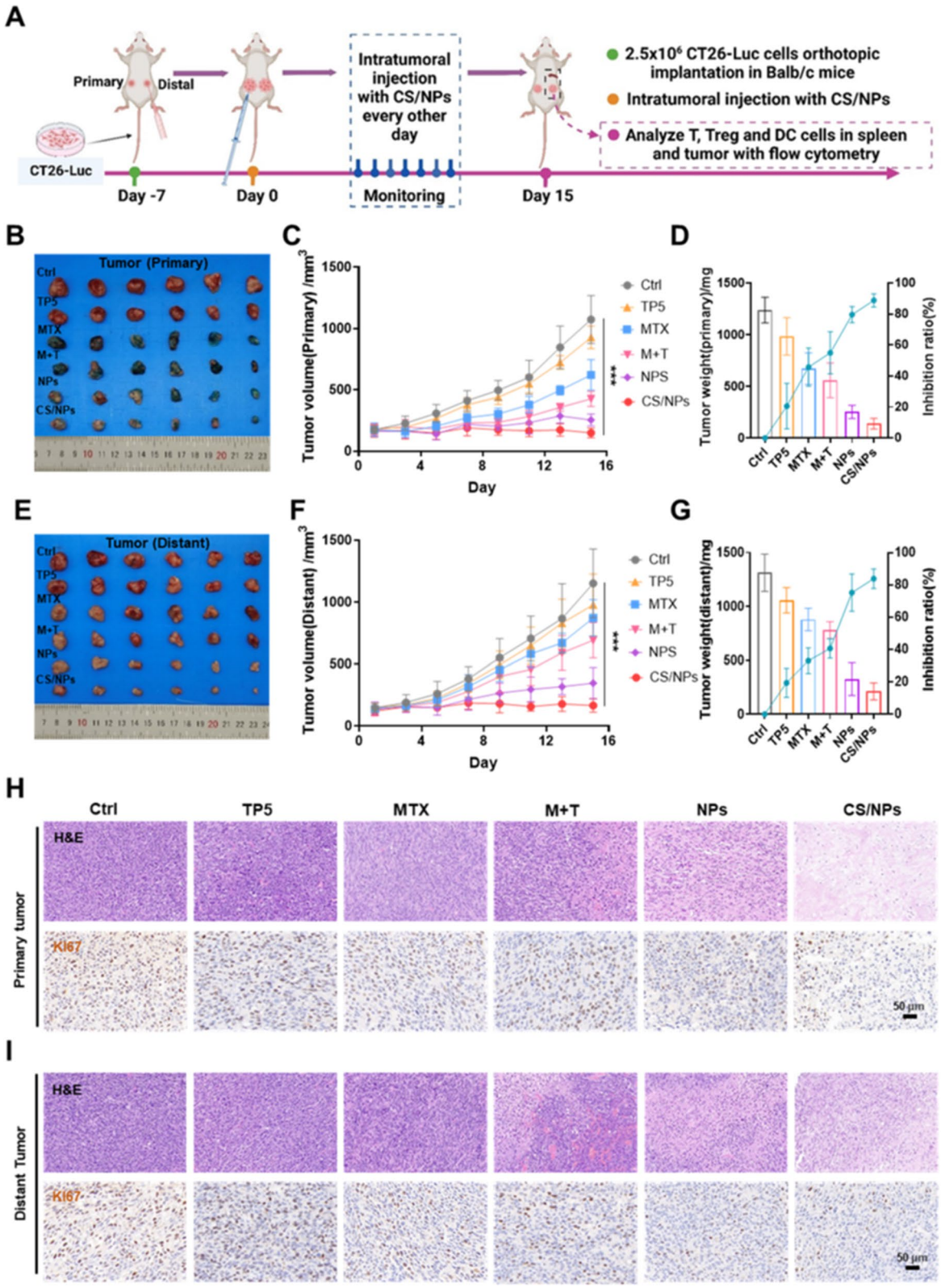

Fig. 6 (See legend on previous page.)

assessed, revealing the significant upregulation of CD80 and/or CD86 (gated by $CD11c^+$ DCs) in the CS/NP treatment group. In addition, CS/NPs treatment reduced the proportion of Treg cells (Figure S4D and Figure S4I, Supporting Information). Altogether, these results suggest that CS/NPs induce an antitumor immune response. In light of these findings, multifunctional nanocomplex CS/NPs demonstrate significant antitumor immune activity and tumor suppression in CRC therapy.

To further investigate the in vivo cGAS-STING pathway activated by CS/NPs, we analyzed the levels of immune response-related cytokines in mouse serum, specifically granzyme B, TNF-α, IL-2, IL-6, IFN-γ, and IL-10. As shown in Fig. 5I–N, the CS/NPs-treated group exhibited significantly increased concentrations of the pro-inflammatory cytokines TNF-α, IFN-γ, IL-2, and IL-6 cytotoxicity-related factor granzyme B compared to the control group. However, the tumor-associated cytokine IL-10 was reduced. These findings demonstrate that CS/NPs activate cGAS-STING signaling to induce tumor-related inflammatory cytokines to be secreted.

Suppression of bilateral tumors by CS/NPs

We employed a bilateral tumor model to validate CS/NPs-mediated CRC immunotherapy (Fig. 6A). The tumor on the left was considered the primary tumor and injected with different treatments, while the tumor on the right was not treated. Mice underwent treatment with an equivalent dose of CS/NPs (2 mg kg^{-1}) injected into the left-side tumor intratumorally every other days for 15 days in total. Mouse weight remained relatively stable (Figure S5A, Supporting Information), indicating the safety of CS/NPs treatment. Treatment with CS/NPs effectively inhibited the volume and weight of both primary (Fig. 6B–D and Figure S5B, Supporting Information) and distant (Fig. 6E–G and Figure S5C, Supporting Information) tumor tissues. Notably, the tumor inhibition rates of both tumors were consistent, which can likely be attributed to systemic immunotherapy (Fig. 6E, G). For example, after treatment with CS/NPs, the average volume of distant tumors (≈170 mm^3) was considerably lower than contral group (≈1150 mm^3). Histological analysis was performed on the primary tumor and distant tumors. The H&E staining results showed extensive necrosis or minimal nuclear staining in both bilateral tumors (Fig. 6H, I). Immunohistochemical staining for Ki67 was conducted, which verified that proliferation was suppressed in both bilateral tumors.

CS/NPs promote a systemic antitumor immune response within the bilateral tumor animal model

This study further investigated whether CS/NPs could initiate an immune response against tumor recurrence. To explore this, this study established a bilateral tumor animal model through injecting CT26-Luc cells into the back of the mouse on both sides. There was a left side primary tumor and a right side distant tumor. The steps conducted during treatment are shown in Fig. 6A. After treatment, the infiltration of mature DC cells and T-cell activation were detected in both primary and distant tumor tissues with flow cytometry and immunofluorescence staining. Treatment with CS/NPs enhanced the proportion of mature DCs that had infiltrated ($CD80^+$/$CD86^+$ cells; Fig. 7A) and caused the significant upregulation of $CD4^+$/$CD8^+$ T-cell in both tumor tissues (Fig. 7B). At the same time, significant suppression was observed in the proportion of Treg cells in the bilateral (Fig. 7C). Combined with the corresponding quantitative data analysis obtained using flow cytometry (Fig. 7D–H), is the results clearly demonstrated that CS/NPs treatment activated the mouse immune system to inhibit distant tumors, in accordance with the outcome of $CD4^+$/$CD8^+$ T-cell immunofluorescence staining (Fig. 7I and Figure S6A, Supporting Information). Moreover, histopathological examination revealed no significant morphological changes in the major organs collected from the CS/NP-treated group (Figure S6B, Supporting Information). Serum biochemical markers (AST and ALT for liver and CRE and urea for kidney) displayed normal fluctuations (Figure S6C–F, Supporting Information), indicating the low side effects of CS/NPs for CRC treatment.

Conclusions

In summary, we have engineered pH-responsive ZIF-8 to encapsulate the chemotherapeutic MTX and immunomodulator TP5. We also functionalized the CRC targeting of CS to obtain CS/NPs that are capable of site-specific delivery and efficient chemo-immunotherapy by activating the cGAS-STING signaling pathway and degrading PD-L1. In this nanoplatform, the coordinated

(See figure on next page.)

Fig. 7 Distant effects of CS/NPs initiation of the cGAS-STING-mediated antitumor immune response in vivo. **A**–**C** Representative flow cytometry images showing mature DC cells ($CD11c^+$-gated $CD80^+$/$CD86^+$ cells), T cells ($CD4^+$/$CD8^+$), and Treg cells recovered from distant tumor tissues after various treatments. **D**–**H** Representative quantitative analysis of mature DC cells ($CD11c^+$-gated $CD80^+$/$CD86^+$ cells), T cells ($CD4^+$/$CD8^+$), and Treg cells in distant tumor tissues following various treatments ($n = 3$). **I** $CD4^+$/$CD8^+$ immunofluorescence staining images of distant tumor tissues in mice following with various treatments, scale bar: 100 μm. $^{**}p < 0.01$; $^{***}p < 0.001$

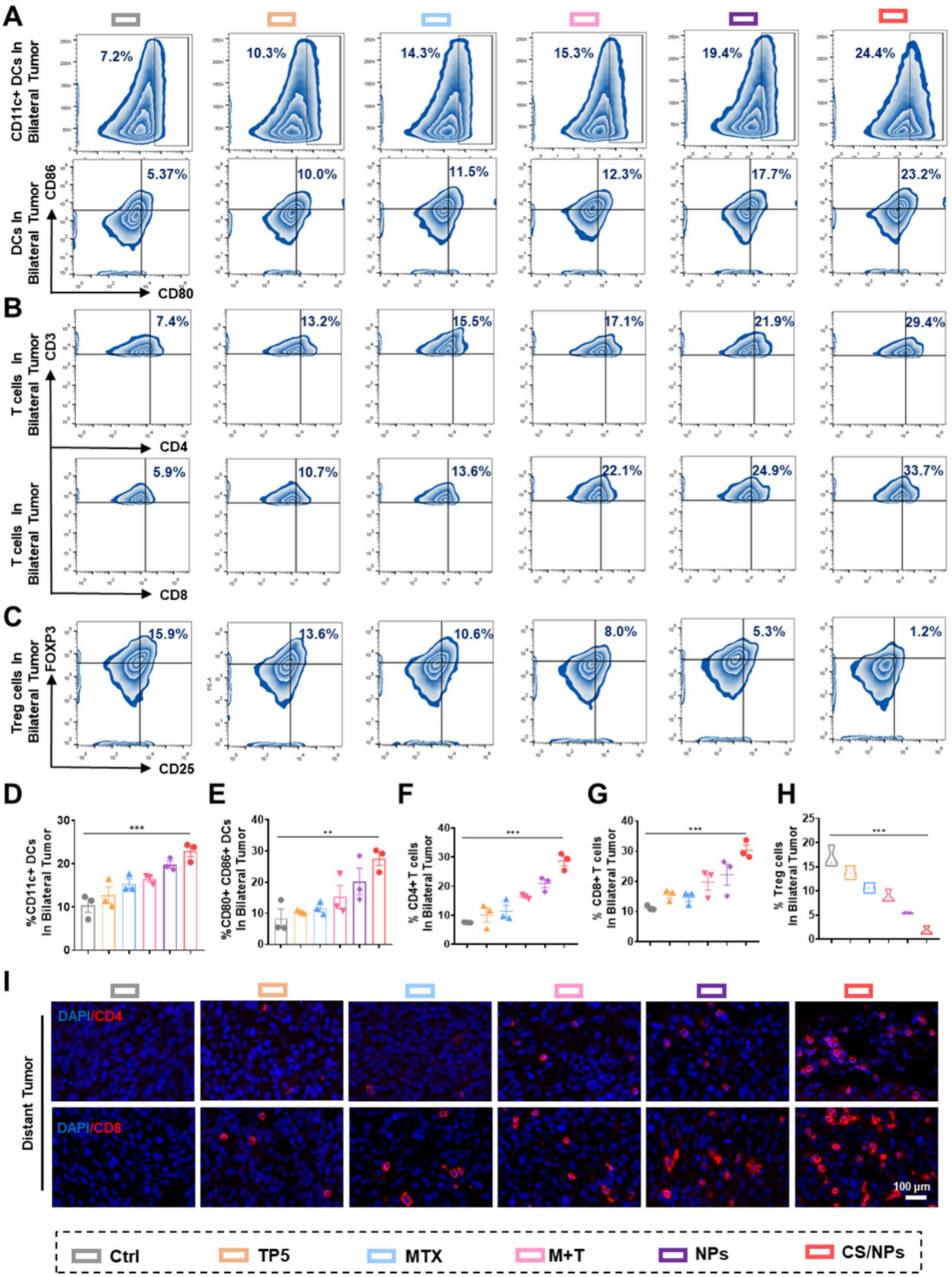

Fig. 7 (See legend on previous page.)

Zn^{2+} effectively disrupts glycolytic processes and downregulates GLUT1 expression, leading to the CRC cells being deprived of their energy supply. This leads to the activation of the AMPK pathway, which mediates the degradation of PD-L1 protein, thereby sensitizing CRC cells toward immunotherapy. Furthermore, MTX treatment damages dsDNA, resulting in the activation of the cGAS-STING pathway which further enhances antitumor immune responses. Moreover, T lymphocytes and DCs are more proliferative and differentiated with TP5, which intensifies the cancer-immunity cycle. Overall, CS/NPs can efficiently sensitize CRC cells toward chemotherapy and promotes systemic antitumor immunity both in vitro and in vivo, thereby represents an novel strategy to a feasible method of CRC chemo-immunotherapy.

Supplementary Information

The online version contains supplementary material available at https://doi.org/10.1186/s12951-024-02836-3.

Supplementary Material 1

Acknowledgements
The authors would like to thank the Pub-lab of West China School of Basic Medical Sciences and Forensic Medicine, Sichuan University, for providing various laboratory instruments.

Author contributions
X.D. Zhang, HL Tian and Y Chen made equal contributions to this work. XD Zhang was mainly responsible for data curation, writing, and preparing the initial draft. HL Tian focused on data management, as well as writing, reviewing, and editing. Y Chen took charge of data organization and analysis, and also participated in writing, reviewing, and editing. B.C. Liang contributed to software operation and research. Ed. Nice and C.H. Huang played a role in writing review and editing. N.Xie, and S.J.Zheng provided key support in methodology, resources, project management, and funding acquisition. All authors reviewed the manuscript.

Funding
This work was supported by grants from the National Natural Science Foundation of China (81960528, 823B2081), the Hainan Province Science and Technology Special Fund (ZDYF2022SHFZ065), the specific research fund of The Innovation Platform for Academicians of Hainan Province (YSPTZX202208), the Hainan Province Clinical Medical Center (QWYH2022341), and 1·3·5 project for disciplines of excellence, West China Hospital, Sichuan University (ZYGD22007).

Data availability
No datasets were generated or analysed during the current study.

Declarations

Ethics approval and consent to participate
All animal experiments conformed to the requirements of the institutional animal use and care system of Sichuan University.

Consent for publication
Not applicable.

Competing interests
The authors declare no competing interests.

Author details
[1]Key Laboratory of Emergency and Trauma of Ministry of Education, Engineering Research Center for Hainan Biological Sample Resources of Major Diseases, The Hainan Branch of National Clinical Research Center for Cancer, the First Clinical College & the First Affiliated Hospital, Hainan Medical University, Haikou 570102, China. [2]Key Laboratory of Tropical Cardiovascular Diseases Research of Hainan Province, Hainan Women and Children's Medical Center, Hainan Medical University, Haikou 571199, China. [3]West China School of Basic Medical Sciences and Forensic Medicine, Sichuan University, and State Key Laboratory of Biotherapy and Cancer Center, West China Hospital, and Collaborative Innovation Center for Biotherapy, Chengdu 610041, China. [4]School of Basic Medical Sciences, State Key Laboratory of Southwestern Chinese Medicine Resources, Chengdu University of Traditional Chinese Medicine, Chengdu 611137, China. [5]Department of Biochemistry and Molecular Biology, Monash University, Clayton, VIC 3800, Australia.

Received: 22 May 2024 Accepted: 4 September 2024
Published online: 30 September 2024

References

1. Dekker E, Tanis PJ, Vleugels JLA, Kasi PM, Wallace MB. Colorectal cancer. Lancet. 2019;394:1467–80.
2. Hossain MS, Karuniawati H, Jairoun AA, Urbi Z, Ooi J, John A, Lim YC, Kibria KMK, Mohiuddin AKM, Ming LC, et al. Colorectal cancer: a review of carcinogenesis, global epidemiology, current challenges, risk factors, preventive and treatment strategies. Cancers. 2022;14:1732.
3. Siegel RL, Miller KD, Fuchs HE, Jemal A. Cancer statistics, 2022. CA Cancer J Clin. 2022;72:7–33.
4. Zhu S, Zhang T, Zheng L, Liu H, Song W, Liu D, Li Z, Pan CX. Combination strategies to maximize the benefits of cancer immunotherapy. J Hematol Oncol. 2021;14:156.
5. Galluzzi L, Humeau J, Buque A, Zitvogel L, Kroemer G. Immunostimulation with chemotherapy in the era of immune checkpoint inhibitors. Nat Rev Clin Oncol. 2020;17:725–41.
6. Decout A, Katz JD, Venkatraman S, Ablasser A. The cGAS-STING pathway as a therapeutic target in inflammatory diseases. Nat Rev Immunol. 2021;21:548–69.
7. Nakajima S, Kaneta A, Kono K. The potential of a novel therapeutic strategy for colorectal cancer targeting the cGAS-STING pathway. Gan Kagaku Ryoho. 2023;50:950–4.
8. Sun L, Wu J, Du F, Chen X, Chen ZJ. Cyclic GMP-AMP synthase is a cytosolic DNA sensor that activates the type I interferon pathway. Science. 2013;339:786–91.
9. Ishikawa H, Ma Z, Barber GN. STING regulates intracellular DNA-mediated, type I interferon-dependent innate immunity. Nature. 2009;461:788–92.
10. Zhou L, Huang Y, Wu Y, Tang S. Nanoparticle targeting cGAS-STING signaling in disease therapy. Nano Res. 2024;17:7315–36.
11. Chen Z, Li S, Li F, Qin C, Li X, Qing G, Wang J, Xia B, Zhang F, Meng L, et al. DNA damage inducer mitoxantrone amplifies synergistic mild-photothermal chemotherapy for TNBC via decreasing heat shock protein 70 expression. Adv Sci (Weinh). 2023;10:e2206707.
12. Evison BJ, Sleebs BE, Watson KG, Phillips DR, Cutts SM. Mitoxantrone, more than just another topoisomerase II poison. Med Res Rev. 2016;36:248–99.
13. Shenkenberg TD, Von Hoff DD. Mitoxantrone: a new anticancer drug with significant clinical activity. Ann Intern Med. 1986;105:67–81.
14. Wang X, Lin M, Zhu L, Ye Z. GAS-STING: a classical DNA recognition pathways to tumor therapy. Front Immunol. 2023;14:1200245.
15. Wang Q, Gao Y, Li Q, He A, Xu Q, Mou Y. Enhancing dendritic cell activation through manganese-coated nanovaccine targeting the cGAS-STING pathway. Int J Nanomed. 2024;19:263–80.
16. Ervin SM, Ramanan SV, Bhatt AP. Relationship between the gut microbiome and systemic chemotherapy. Dig Dis Sci. 2020;65:874–84.
17. Van der Jeught K, Xu HC, Li YJ, Lu XB, Ji G. Drug resistance and new therapies in colorectal cancer. World J Gastroenterol. 2018;24:3834–48.
18. Goldstein G, Audhya TK. Thymopoietin to thymopentin: experimental studies. Surv Immunol Res. 1985;4(Suppl 1):1–10.

19. Zhang T, Qin XY, Cao X, Li WH, Gong T, Zhang ZR. Thymopentin-loaded phospholipid-based phase separation gel with long-lasting immunomodulatory effects: in vitro and in vivo studies. Acta Pharmacol Sin. 2019;40:514–21.
20. Ding N, He K, Tian H, Li L, Li Q, Lu S, Ding K, Liu J, Nice EC, Zhang W, et al. Carrier-free delivery of thymopentin-regulated injectable nanogels via an enhanced cancer immunity cycle against melanoma metastasis. Mater Today Bio. 2023;20:100645.
21. Wang Q, Sun Y, Li S, Zhang P, Yao Q. Synthesis and modification of ZIF-8 and its application in drug delivery and tumor therapy. RSC Adv. 2020;10:37600–20.
22. Maleki A, Shahbazi MA, Alinezhad V, Santos HA. The progress and prospect of zeolitic imidazolate frameworks in cancer therapy, antibacterial activity, and biomineralization. Adv Healthc Mater. 2020;9:e2000248.
23. Parrott D, Suh EH, Khalighinejad P, Jordan VC, Arreola I, Lo ST, Sherry AD. Investigations into the signaling pathways involving glucose-stimulated zinc secretion (GSZS) from prostate epithelial cells in Vitro and in vivo. Mol Imaging Biol. 2023;25:935–43.
24. Costello LC, Franklin RB. Cytotoxic/tumor suppressor role of zinc for the treatment of cancer: an enigma and an opportunity. Expert Rev Anticancer Ther. 2012;12:121–8.
25. Wu S, Zhang K, Liang Y, Wei Y, An J, Wang Y, Yang J, Zhang H, Zhang Z, Liu J, Shi J. Nano-enabled tumor systematic energy exhaustion via zinc (II) interference mediated glycolysis inhibition and specific GLUT1 depletion. Adv Sci (Weinh). 2022;9:e2103534.
26. Meng Y, Xu X, Luan H, Li L, Dai W, Li Z, Bian J. The progress and development of GLUT1 inhibitors targeting cancer energy metabolism. Future Med Chem. 2019;11:2333–52.
27. Hardie DG, Ross FA, Hawley SA. AMPK: a nutrient and energy sensor that maintains energy homeostasis. Nat Rev Mol Cell Biol. 2012;13:251–62.
28. Lin SC, Hardie DG. AMPK: sensing glucose as well as cellular energy status. Cell Metab. 2018;27:299–313.
29. Cha JH, Yang WH, Xia W, Wei Y, Chan LC, Lim SO, Li CW, Kim T, Chang SS, Lee HH, et al. Metformin promotes antitumor immunity via endoplasmic-reticulum-associated degradation of PD-L1. Mol Cell. 2018;71:606-e620607.
30. Zhang R, Yang Y, Dong W, Lin M, He J, Zhang X, Tian T, Yang Y, Chen K, Lei QY, et al. D-mannose facilitates immunotherapy and radiotherapy of triple-negative breast cancer via degradation of PD-L1. Proc Natl Acad Sci USA. 2022;119:e2114851119.
31. Riley RS, June CH, Langer R, Mitchell MJ. Delivery technologies for cancer immunotherapy. Nat Rev Drug Discov. 2019;18:175–96.
32. Ding B, Chen H, Tan J, Meng Q, Zheng P, Ma P, Lin J. ZIF-8 nanoparticles evoke pyroptosis for high-efficiency cancer immunotherapy. Angew Chem Int Ed Engl. 2023;62:e202215307.
33. Pothuraju R, Rachagani S, Krishn SR, Chaudhary S, Nimmakayala RK, Siddiqui JA, Ganguly K, Lakshmanan I, Cox JL, Mallya K, et al. Molecular implications of MUC5AC-CD44 axis in colorectal cancer progression and chemoresistance. Mol Cancer. 2020;19:37.
34. Muller S, Sindikubwabo F, Caneque T, Lafon A, Versini A, Lombard B, Loew D, Wu TD, Ginestier C, Charafe-Jauffret E, et al. CD44 regulates epigenetic plasticity by mediating iron endocytosis. Nat Chem. 2020;12:929–38.
35. Andrade F, Rafael D, Vilar-Hernandez M, Montero S, Martinez-Trucharte F, Seras-Franzoso J, Diaz-Riascos ZV, Boullosa A, Garcia-Aranda N, Camara-Sanchez P, et al. Polymeric micelles targeted against CD44v6 receptor increase niclosamide efficacy against colorectal cancer stem cells and reduce circulating tumor cells in vivo. J Control Release. 2021;331:198–212.
36. Azimijou N, Karimi-Soflou R, Karkhaneh A. CD44 targeted-chondroitin sulfate nanoparticles: fine-tuning hydrophobic groups to enhance in vitro pH-responsiveness and in vivo efficacy for advanced breast cancer treatment. Biomater Adv. 2024;158:213776.
37. Amhare AF, Lei J, Deng H, Lv Y, Han J, Zhang L. Biomedical application of chondroitin sulfate with nanoparticles in drug delivery systems: systematic review. J Drug Target. 2021;29:259–68.
38. Drijvers E, Liu J, Harizaj A, Wiesner U, Braeckmans K, Hens Z, Aubert T. Efficient endocytosis of inorganic nanoparticles with Zwitterionic surface functionalization. ACS Appl Mater Interfaces. 2019;11:38475–82.
39. Bellosillo B, Colomer D, Pons G, Gil J. Mitoxantrone, a topoisomerase II inhibitor, induces apoptosis of B-chronic lymphocytic leukaemia cells. Br J Haematol. 1998;100:142–6.
40. Koceva-Chyla A, Jedrzejczak M, Skierski J, Kania K, Jozwiak Z. Mechanisms of induction of apoptosis by anthraquinone anticancer drugs aclarubicin and mitoxantrone in comparison with doxorubicin: relation to drug cytotoxicity and caspase-3 activation. Apoptosis. 2005;10:1497–514.
41. Bhuyan PK, Dallas M, Kraynyak K, Herring T, Morrow M, Boyer J, Duff S, Kim J, Weiner DB. Durability of response to VGX-3100 treatment of HPV16/18 positive cervical HSIL. Hum Vaccin Immunother. 2021;17:1288–93.
42. Morrow MP, Kraynyak KA, Sylvester AJ, Shen X, Amante D, Sakata L, Parker L, Yan J, Boyer J, Roh C, et al. Augmentation of cellular and humoral immune responses to HPV16 and HPV18 E6 and E7 antigens by VGX-3100. Mol Ther Oncolytics. 2016;3:16025.
43. Mascola JR, Fauci AS. Novel vaccine technologies for the 21st century. Nat Rev Immunol. 2020;20:87–8.
44. Zhang R, Yang W, Zhu H, Zhai J, Xue M, Zheng C. NLRC4 promotes the cGAS-STING signaling pathway by facilitating CBL-mediated K63-linked polyubiquitination of TBK1. J Med Virol. 2023;95:e29013.
45. Yoshimura A, Aki D, Ito M. SOCS, SPRED, and NR4a: negative regulators of cytokine signaling and transcription in immune tolerance. Proc Jpn Acad Ser B Phys Biol Sci. 2021;97:277–91.
46. Tay C, Tanaka A, Sakaguchi S. Tumor-infiltrating regulatory T cells as targets of cancer immunotherapy. Cancer Cell. 2023;41:450–65.
47. Nie P, Cao Z, Yu R, Dong C, Zhang W, Meng Y, Zhang H, Pan Y, Tong Z, Jiang X, et al. Targeting p97-Npl4 interaction inhibits tumor T(reg) cell development to enhance tumor immunity. Nat Immunol. 2024;25:1623–36.

Publisher's note